Enhanced Resolution ERS-1 Scatterometer Imaging of Southern Hemisphere Polar Ice

David G. Long and David S. Early
Brigham Young University
459 Clyde Building
Provo, UT 84602

Mark R. Drinkwater
Jet Propulsion Laboratory, California Institute of Technology
MS 300-323 4800 Oak Grove Dr.
Pasadena, CA 91109

Abstract - The ERS-1 mission has generated a wealth of radar data over the Southern Hemisphere polar region. While the SAR mode of the ERS-1 Active Microwave Instrument (AMI) can provide only limited temporal and spatial coverage, the scatterometer mode provides frequent, global coverage, albeit at a much lower (50 km) resolution. By applying a recently developed algorithm for generating enhanced resolution scatterometer images, the ERS-1 scatterometer data can be used to study both sea ice and glacial ice to support SAR-based studies. This paper describes the algorithm and its application to ERS-1 scatterometer data with particular emphasis on sea ice. Selected images from a time series covering a complete annual cycle are presented.

I. INTRODUCTION

The narrow swath and data rate and power requirements of the ERS-1 AMI SAR limit its coverage of the polar region. However, the AMI scatterometer mode, designed primarily for oceanic wind measurements, provides a 500 km wide coverage swath and frequent, global coverage at 50 km resolution. An algorithm for generating enhanced resolution images from scatterometer data has recently been developed to enable the effective use of scatterometer measurements in land and ice studies.

In this paper the algorithm is applied to create enhanced resolution images from ERS-1 scatterometer data over the entire Southern Hemisphere Polar region. The resulting images are time-integrated maps of the mean radar backscatter coefficient normalized to 40° incidence angle (termed "$\mathcal{A}$") over a seven day period. Separate images are made of the dependence of the backscatter on incidence angle. A time series of these medium-scale $\mathcal{A}$ images of Antarctica and the surrounding seas is presented. Such images complement the lower frequency temporal and spatial coverage of the high resolution SAR images. We describe the application of the algorithm to ERS-1 scatterometer data and discuss the relative strengths of the resolution enhancement algorithm applied to scatterometer data for the study of sea ice. Additional results are given in separate papers (Early et al., 1994; Drinkwater et al., 1993; 1994).

II. SCATTEROMETER IMAGING

The wide AMI scatterometer swath provides frequent, multiple-incidence angle coverage of the polar region in a given location. The scatterometer mode operates essentially continuously whenever the AMI SAR mode is not in use. Until recently, the intrinsic low resolution of the scatterometer data has limited its application in ice studies. However, applying a resolution enhancement algorithm permits the generation of weekly images of the entire Southern Ocean sea-ice cover at a resolution higher than present alternatives. The resulting backscatter images are based on multiple azimuth and incidence angle observations. This diversity is helpful in ice characteristics discrimination and in the separation of ice from ocean.

Long et al. (1993) developed an algorithm for generating enhanced resolution images from scatterometer data. This algorithm was developed expressly for Seasat scatterometer (SASS) data but, with suitable modifications, can be applied to ERS-1 scatterometer data. The algorithm is based upon the spatial overlap achieved by the instrument over a period of time (multiple orbits). The algorithm has been successfully applied to the study of glacial ice using SASS over Greenland by Long and Drinkwater (1994) [see also Early et al. (1994)].

With respect to the resolution enhancement algorithm, the key difference between SASS and ERS-1 is the spatial response of the measurements and the spatial filter applied to the ERS-1 measurements. Each ERS-1 scatterometer measurement of the radar backscatter (σ^o) consists of a series of pulses which are integrated and spatially filtered. The nominally 50 km resolution σ^o measurements are reported on a 25 km grid; however, the number and relative positions of the pulses integrated into a given σ^o measurement are variable, reducing the effective resolution enhancement capability of the algorithm. The spacecraft passes over a given region on either an ascending or descending ground track every few orbits. In general, a given area at high latitudes is generally observed several times each day with varying azimuth and incidence angles.

Backscatter from ice is a function of the measurement incidence angle, θ, and geophysical properties of the ice. In the incidence angle range $18° \leq \theta \leq 60°$, corresponding to the range of scatterometer measurements, σ^o (in dB) is approximately a linear function of θ

$$10 \log_{10} \sigma^o(\theta) = \mathcal{A} + \mathcal{B}(\theta - 40°) \tag{1}$$

where the coefficients $\mathcal{A}$ and $\mathcal{B}$ depend on the ice characteristics. $\mathcal{A}$ is the 40° incidence angle-normalized σ^o, while $\mathcal{B}$ describes the dependence of σ^o on θ. Note that 40° represents the mean θ of the observations and is thus a convenient angle for making comparative data analyses.

Over sea ice, the azimuthal modulation of σ^o is typically less than 1.0 dB: in subsequent processing σ^o was assumed to have no azimuth-angle modulation. Ignoring such modulation is recognized as a limitation of this current work, as open water or low ice concentration areas may be present within the pack where surface scattering from wind-generated capillary waves can result in different σ^o values between the three beams.

III. RESOLUTION ENHANCMENT ALGORITHM

The scatterometer image reconstruction algorithm with filtering (SIRF) as applied to SASS is described in detail by Long et al. (1993). The technique utilizes multiple, overlapping measurements of σ^o and signal processing techniques to generate images of $\mathcal{A}$ and $\mathcal{B}$ which can have better resolution than the intrinsic σ^o measurement resolution. For SASS, SIRF provides images of $\mathcal{A}$ and $\mathcal{B}$ with a resolution of up to 4-5 km from originally 50 km resolution measurements (Long et al., 1993).

The effective enhancement is dependent on the spatial response and overlap of the measurements from different passes, the response of the spatial filter applied to the original pulse measurements, and the spatial accuracy of the gridded scatterometer data. The resolution enhancement achieved with ERS-1 scatterometer data is limited by the spatial filter applied to the data and the lack of knowledge of the individual pulse locations after interpolation to a fixed grid.

SIRF utilizes a small-scale rectilinear grid of resolution elements on the earth's surface. As the fore, mid and aft beams successively sweep over the grid, the overlapping measurement cells of each of the three antennae are superimposed upon the grid elements. The estimated value of backscatter ϱ_k for the k^{th} measurement is a weighted average of the σ^o values of the individual resolution elements covered by the integration measurement cell, i.e.,

$$\varrho_k = \sum \sum h(x, y; k) \sigma^o(x, y; k) \tag{2}$$

where the summations are defined over the non-zero values of the weighting function $h(x, y; k)$ corresponding to the measurement response. The measurement response includes the antenna gain pattern and filter responses.

Since actual scatterometer measurements are noisy, the technique is extended to include noise effects. A modified, multivariate multiplicative algebraic reconstruction technique (MART) with a nonlinear update is used to compute the high resolution estimates of $\mathcal{A}$ and $\mathcal{B}$ using Eq. (1). The iterative algorithm results in enhanced resolution images of A and B where each grid resolution element becomes a pixel in the reconstructed image.

An initial $\mathcal{B}$ estimate image, $\mathcal{B}^0$, is made by setting $b_i^0 = -0.13$ dB/deg (the global average of $\mathcal{B}$) where i is the row-order pixel number. The initial $\mathcal{A}$ image is set to zero, i.e., $a_i^0 = 0$. In the k^{th} iteration, the previous $\mathcal{B}$ estimate image is used to generate an estimate of $\mathcal{A}$. Linear regression of the $\mathcal{A}$ update terms (expressed at the original measurement incidence angle) is then used to update the previous estimate of $\mathcal{B}$. To improve noise tolerance, both the new $\mathcal{A}$ and $\mathcal{B}$ estimates are determined as a non-linearly weighted average of the previous estimates and the estimate update.

With the σ^o measurements expressed in dB, z_j, the scatterometer image reconstruction (SIR) algorithm follows. Define

$$f_j^k = 10\log_{10}\left[\frac{1}{p_i}\sum_{n=1}^{N} h_{jn}10^{a_n^k/10}\right], \quad p_i = \sum_{m=1}^{N} h_{mi}, \tag{3}$$

$$d_{ij}^k = \left(\frac{z_j - b_i^k(\theta_j - 40°)}{f_j^k}\right)^w, \quad r_i = \sum_{j=1}^{N} h_{ji}\theta_j^2, \ \text{and} \ t_i = \sum_{j=1}^{N} h_{ji}\theta_j. \tag{4}$$

The $\mathcal{A}$ estimate update term, u_{ij}^k, is computed as

$$u_{ij}^k = \begin{cases} \left[\frac{1}{2}\frac{1}{f_j^k}\left(1 - \frac{1}{d_{ij}^k}\right) + \frac{1}{a_i^k d_{ij}^k}\right]^{-1} & d_{ij}^k \geq 1 \\ \left[\frac{1}{2}f_j^k\left(1 - d_{ij}^k\right) + a_i^k d_{ij}^k\right] & d_{ij}^k < 1 \end{cases} \tag{5}$$

with the $\mathcal{A}$ estimate, a_i^k, updated according to

$$a_i^{k+1} = \frac{1}{p_i}\sum_{j=1}^{N} h_{ji}u_{ij}^k. \tag{6}$$

Linear regression of the $\mathcal{A}$ updates, u_{ij}^k, provides an update for $\mathcal{B}$,

$$c_i^k = \frac{1}{p_i r_i - t_i^2}\left(p_i\sum_{j=1}^{N} h_{ji}\theta_j\zeta_{ij}^k - t_i\sum_{j=1}^{N} h_{ji}\zeta_{ij}^k\right). \tag{7}$$

where $\zeta_{ij}^k = u_{ij}^k + b_i^k(\theta_j - 40°)$. The $\mathcal{B}$ estimate is updated using a weighted average of c_i^k and the previous $\mathcal{B}$ estimate,

$$b_i^{k+1} = \frac{1}{r+1}\left(rc_i^k + b_i^k\right) \quad \text{where} \quad r = \frac{p_i}{t_i^2}\sum_{j=1}^{N} h_{ji}\theta_j^2 - 1. \tag{8}$$

This system of equations is iterated over k until convergence (typically 20-40 iterations for ERS-1). The subjective quality of the final images is improved by applying a hybrid median-linear filter to the image estimates at each stage of the iteration (Long et al., 1993).

For SASS, sufficient resolution enhancement is obtained by using a simplifed binary-valued h where h is set to unity within the 3dB cell response and zero outside. To maximize the resolution enhancement of ERS-1 scatterometer data the spatial response function of the ERS-1 σ^o measurements is used where the response function is a circular $\cos^2$ with the 3 dB point at 50 km diameter (see Fig. 1). Improved knowledge of the response function, the pulse locations, and the pulse interpolation function would significantly improve the resolution enhancement capability.

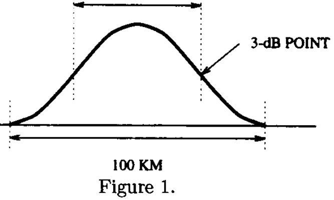

Figure 1.
Slice through the ERS-1 σ^o measurement response.

IV. SCATTEROMETER IMAGING CONSIDERATIONS

In this study an equal-area Lambert image projection is used and the resulting image pixel resolution is chosen to be approximately 12 km. The resolution enhancement is not without cost since variance in the $\mathcal{A}$ and $\mathcal{B}$ images increases as resolution is increased. Thus, a tradeoff must be made between the resolution and the noise level with multiple passes over the target required to obtain sufficient measurement overlap for the reconstruction algorithm to yield a resolution improvement. The absolute resolution improvement depends on the measurement response and the total number of measurements, with greater numbers contributing to a reduced estimate of noise and/or improved resolution. In addition, during the "imaging time interval" the radar and surface characteristics must remain constant between passes. Thus, some tradeoff must be made between imaging time interval and resolution, due to temporal change. Other requirements are imposed and additional assumptions made regarding the σ^o measurements, including: (i) Instrument calibration must remain stable over the data acquisition interval. (ii) σ^o is assumed independent of the azimuth angle of the measurement. (iii) Surface topographic effects on the image reconstruction process are assumed negligible and are ignored.

Large long-term seasonal changes are observed in $\mathcal{A}$ and $\mathcal{B}$ in sea ice regions over a full ice growth year in the Southern Ocean. In contrast, however, the large-scale relative change in σ^o over 1 to 2 weeks is relatively small and so we restrict the imaging interval to 1 week. A seven day imaging time interval obtains the best trade-off between coverage and resolution. Resulting images reflect the average or 'filtered' sea-ice backscatter response during this imaging time period. Variations in σ^o during each 1 week interval are treated as noise by the image reconstruction algorithm. Thus, short-term variability (timescales < 7 d) is averaged out and only the longer timescale changes due to the large-scale sea ice dynamics remain in the weekly images.

A major drawback of this approach is the assumption that sea ice motion is not important in the image reconstruction: these effects are under investigation. Measurements of sea-ice floe drift rates indicate typical mean drift displacement of around the equivalent of $\sim 5 \pm 3$ pixels/week in the reconstructed weekly images. This smoothes any remaining high frequency pixel variability in the final images. The resulting medium-scale images nonetheless have significant application to sea-ice geophysical studies and are illustrated in the following section.

V. IMAGE TIME SERIES

Time-series maps of the Southern Ocean are a primary application of the SIRF imaging technique. The capability of the SIRF algorithm to produce images of the sea-ice characteristics around the whole Antarctic Continent is demonstrated in Figures 2 and 3. Figure 2 is an image of the sea-ice at nearly the minimum ice extent, during the first week of February 1992 (Julian Days 32-38). Figure 3 shows the contrasting situation near maximum ice extent at the end of September 1992 (Julian Days 272-278).

Both images show smoothly varying isotropic returns from the sea ice in contrast to the highly variable and anisotropic returns of the ocean beyond the sea ice margin around Antarctica (due to backscattering from wind-generated waves). The residual Antarctic sea-ice cover in the Amundsen, Bellingshausen and Weddell Seas is clearly marked in Figure 2 as bright patches extending northwards from the Antarctic coast. Figure 3 clearly shows the regions of greatest ice extent during winter with the lower mean $\mathcal{A}$ values of winter sea-ice evident. Note the contrastingly greater structure observed within this extensive sea ice cover with particularly strong swirls and bands observed in the backscatter values of the Weddell Sea.

The C-band backscatter at 40° incidence angle largely reflects the salinity and roughness of the sea ice (Drinkwater et al., 1994). Both of these sea-ice geophysical properties are related to the age of the sea ice and its history of deformation throughout a single ice season. Another factor may be snow depth, which is also related to the age of the ice since formation. Summer $\mathcal{A}$ values in Fig. 2 reach -10 dB owing to predominantly rough surface scattering from ice floes during wet surface conditions. In contrast, the mean winter $\mathcal{A}$ values in Fig. 3 decrease, as a higher salinity first-year ice cover grows rapidly to latitudes north of 60° S near the Greenwich meridian. A more detailed study of the scattering characteristics of the Weddell Sea area is given in Drinkwater et al. (1994).

VI. SUMMARY

The approach discussed here for generating weekly ERS-1 sea ice images for the entire Northern or Southern polar regions provides a valuable supplement to the spatially and temporally sparse higher resolution SAR images. The enhanced ERS-1 scatterometer images provide (1) frequent global coverage and (2) multiple incidence angle observations. While the latter capability is not investigated here, the images of backscatter normalized to 40° incidence provide a remarkable capability for monitoring basin-wide processes. A relative improvement in the spatial accuracy and knowledge of the individual pulse locations within the scatterometer products would further improve the spatial and temporal resolution of these products.

ACKNOWLEDGEMENTS

This work was supported by the National Aeronautics and Space Administration (NASA) by Dr. Robert Thomas. Part of this work (MRD) was carried out at the Jet Propulsion Laboratory, California Institute of Technology, under contract to NASA, with the remainder (DGL and DSE) conducted at Brigham Young University. We thank ESA for the use of the data. MRD carried out this research as one component within the PIPOR Study PIP.Ant3.

REFERENCES

Early, D.E., D.G. Long, and M.R. Drinkwater,"Comparison of Enhanced Resolution Images of Greenland from the ERS-1 and Seasat Scatterometers," in IGARSS Digest, 1994.

Drinkwater, M.R., D.E. Early, and D.G. Long, "ERS-1 Investigations of Southern Ocean Sea Ice Geophysics using Combined Scatterometer and SAR Images," in IGARSS Digest, 1994.

Drinkwater, M.R., D.G. Long, and D.E. Early, "Enhanced-Resolution ERS-1 Imaging of Southern-Ocean Sea Ice," *ESA Journal*, Vol. 17, pp. 307-322, 1993.

Long, D.G., and M.R. Drinkwater, "Greenland Ice Sheet Surface Properties Observed by the Seasat-A Scatterometer at Enhanced Resolution," *J. Glaciology*, In Press, 1994.

Long, D.G., P.J. Hardin, and P.T. Whiting, "Resolution Enhancement of Spaceborne Scatterometer Data," *IEEE Trans. Geosci. Remote Sens.*, Vol. 31, No. 3, pp. 700-715, 1993.

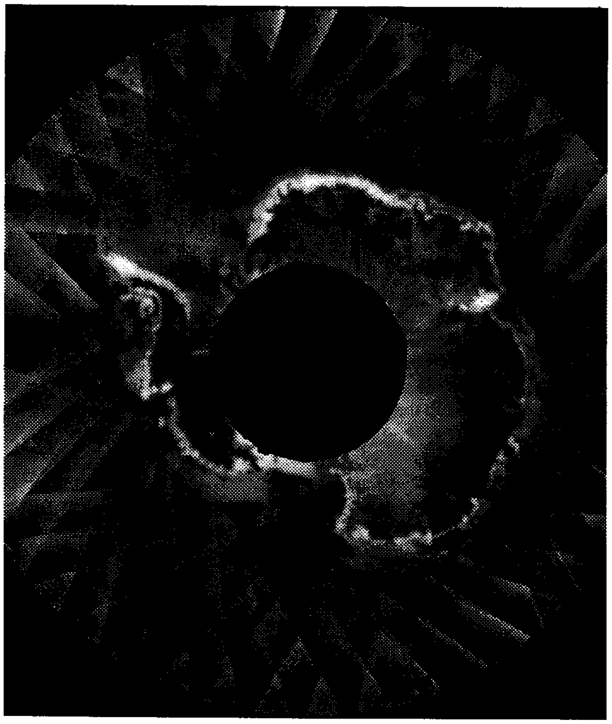

Figure 2.
$\mathcal{A}$ image (σ^o at 40° incidence angle) for JD 32-38, 1992. Data copyright ESA 1992.

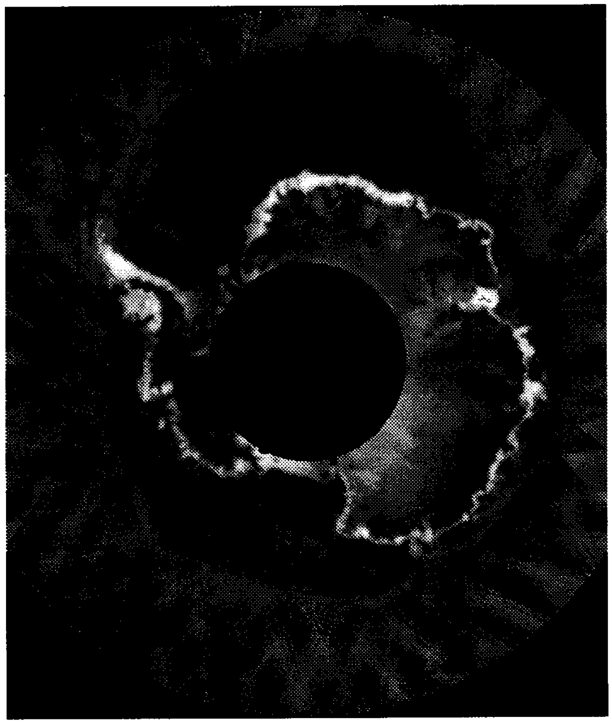

Figure 3.
$\mathcal{A}$ image (σ^o at 40° incidence angle) for JD 272-278, 1992. Data copyright ESA 1992.